On the Mechanisms of Rain Formation in an Idealized Supercell Storm

MATTHEW R. KUMJIAN

Department of Meteorology, The Pennsylvania State University, University Park, Pennsylvania

ZACHARY J. LEBO

Cooperative Institute for Research in Environmental Sciences, University of Colorado, and NOAA/Earth System Research Laboratory, Chemical Sciences Division, Boulder, Colorado

HUGHBERT C. MORRISON

Mesoscale and Microscale Meteorology Division, National Center for Atmospheric Research, Boulder, Colorado*

(Manuscript received 9 December 2014, in final form 27 February 2015)

ABSTRACT

Deep convective storms produce raindrops through three mechanisms: condensation and coalescence growth of cloud liquid droplets (i.e., warm processes), melting of ice hydrometeors, and shedding from wet hailstones. To investigate the relative importance of these mechanisms and their contributions to exotic drop size distributions (DSDs) observed near the surface in supercell storms, an idealized simulation of a supercell is performed using a modified version of the Morrison two-moment microphysics scheme. The modified scheme includes separate categories for warm, shed, and melted rain.

Rain originating from melting ice dominates the rain mass at low levels, especially along the right forward-flank precipitation shield, whereas shed-rain drops dominate a region within the left forward flank. Warm rain is only dominant in the upshear portion of the rear flank of the storm at low levels, though it dominates the total rain mass within the main updraft aloft. The warm-rain mass at low levels is associated with strong low-level downdrafts, consistent with previously published hypotheses based on polarimetric radar observations. Raindrops produced via warm processes are smaller on average than those produced by shedding and melting; drops in the latter class tend to be the largest.

Overall, the simulations fail to reproduce the diverse nature of observed supercell DSDs, although the modified microphysics scheme does increase the variability of surface DSDs compared to the Control run. This implies that more sophisticated treatment of rain microphysics is needed to capture the natural variability of supercell DSDs, including the ability to evolve the DSD spectral shape through sedimentation and collisional processes.

1. Introduction

Recent research has demonstrated that the thermodynamic properties of supercell rear-flank downdraft (RFD) air contribute to whether or not a storm produces a tornado (e.g., Markowski et al. 2002, 2003; Grzych et al. 2007; Lee et al. 2011, 2012). Precipitation processes are a large driver of these RFD thermodynamic properties because melting of hail and graupel, evaporation of rain, and precipitation particles imparting drag on the air contribute to negative buoyancy and thus to downdrafts. Therefore, the precipitation properties of supercell RFDs and hook echoes have been of interest (e.g., Kumjian 2011; French et al. 2014, 2015).

Polarimetric radar observations of supercells and RFDs in particular have revealed "exotic" particle size distributions at low levels (e.g., Kumjian 2011), including a preponderance of large raindrops along the forward flank and a large gradient in median drop sizes across the hook echo and RFD regions. The rear portion of hook echoes (and sometimes wrapping around the

* The National Center for Atmospheric Research is sponsored by the National Science Foundation.

Corresponding author address: Dr. Matthew Kumjian, Department of Meteorology, The Pennsylvania State University, 513 Walker Building, University Park, PA 16801.
E-mail: kumjian@psu.edu

DOI: 10.1175/MWR-D-14-00402.1

south side of the low-level circulation) is often characterized by drop size distributions (DSDs) heavily skewed toward smaller drops with concentrations that are much larger than is typical of convective rain in Oklahoma (Kumjian 2011). It was hypothesized that warm-rain processes lead to the generation of these small drops, which are then transported toward the surface by dynamically driven downdrafts. This type of mechanism would lead to a link between RFD surges and microphysical properties of the RFD. More recently, high-resolution polarimetric radar observations by French et al. (2015) generally support these findings and add to a small but growing dataset of observations suggesting microphysical differences between the hook echoes of tornadic and nontornadic storms (e.g., Kumjian and Ryzhkov 2008a). In particular, French et al. (2015) found that observations of small drops were more frequent in tornadic hook echoes than in nontornadic hook echoes and in environments characterized by higher surface relative humidity and lower environmental lifting condensation levels (LCLs).

Although only limited data are available from surface disdrometers in supercells, the measurements are in good agreement with inferences made from polarimetric radar data (e.g., Schuur et al. 2001; Dawson and Romine 2010). Schuur et al. (2001) found a sparse population of very large raindrops along the forward flank in a supercell, followed by a very large concentration of small drops (more numerous than in any other storm type they investigated) in the rear portion of the supercell and/or RFD. Dawson and Romine (2010) also found a gradient in mean drop size across the hook echo, with large drops located along the leading edge and smaller drops in the rear portion.

In convective storms, raindrops form via three mechanisms: (i) autoconversion of cloud droplets into rain, or what we will call ''warm-rain'' generation; (ii) melting of ice particles such as snow, graupel, and hail; and (iii) shedding of excess water off hailstones that are melting or undergoing wet growth in updrafts. Rain that reaches the surface may originate from any combination of these processes. However, the different mechanisms tend to produce different DSDs; for example, shed drops tend to be smaller in size (~1 mm) with a narrow distribution (e.g., Rasmussen et al. 1984; Rasmussen and Heymsfield 1987), whereas melting of small hailstones can contribute to very large (up to ~8 mm) raindrops (e.g., Rasmussen et al. 1984; Ryzhkov et al. 2013). Thus, the different rain generation mechanisms can produce very different DSDs, which may be sorted and advected to various portions of the storm by the complex three-dimensional airflow patterns typical of supercells, resulting in exotic surface DSDs, or those deviating significantly from what is expected in continental convective storms (Kumjian 2011).

Such exotic surface DSDs cannot be simulated with most existing bulk microphysical schemes because rain is typically treated as a single hydrometeor class with a particle size distribution (PSD) shape prescribed a priori. (This shape is usually an exponential or gamma-type distribution.) This places a rigid constraint on the possible DSD shapes attainable in simulated storms. An additional prognostic moment is required to allow the PSD shape to evolve. Recently, use of such three-moment schemes has been gaining popularity. For example, the three-moment scheme of Milbrandt and Yau (2005b) predicts the spectral shape parameter, allowing DSDs to broaden or narrow under the influence of microphysical processes, especially for sedimentation. Other examples include studies by Dawson et al. (2014), Loftus et al. (2014) for hail, and Van Den Broeke (2014). Still, however, a functional form of the DSD is prescribed a priori; therefore, simulating unusual DSDs comprising raindrops originating by different mechanisms is not possible. An exception is the recent microphysics scheme developed by Prof. J. Straka (2012, personal communication), which was used in the study of Van Den Broeke and Straka (2010) and Van Den Broeke (2014), and is a first step in treating rain DSDs in a more sophisticated manner in bulk parameterizations. This scheme uses three different rain classes to reflect the varied mechanisms that produce rain in deep convective storms, as well as two additional liquid hydrometeor categories (cloud droplets and drizzle). We adopt a similar technique in the present study in an effort to explore the source of rain in different regions of an idealized supercell and how these different sources contribute to the total combined DSD near the surface. The details of the numerical model and the microphysics scheme are provided in the next section. Section 3 compares the standard idealized supercell simulation setup to the simulation with modified microphysics. Section 4 presents an analysis of the results of the simulation using the modified microphysics scheme, with a discussion in section 5 and conclusions given in section 6.

2. Model

a. *Microphysics scheme*

The baseline simulation in this study uses the two-moment Morrison microphysics scheme (Morrison et al. 2005, 2009; Morrison and Milbrandt 2011, hereafter ''Control''), which predicts the mass and number mixing ratios of cloud droplets, raindrops, cloud ice, snow, and a rimed ice category. For this study, the denser option is

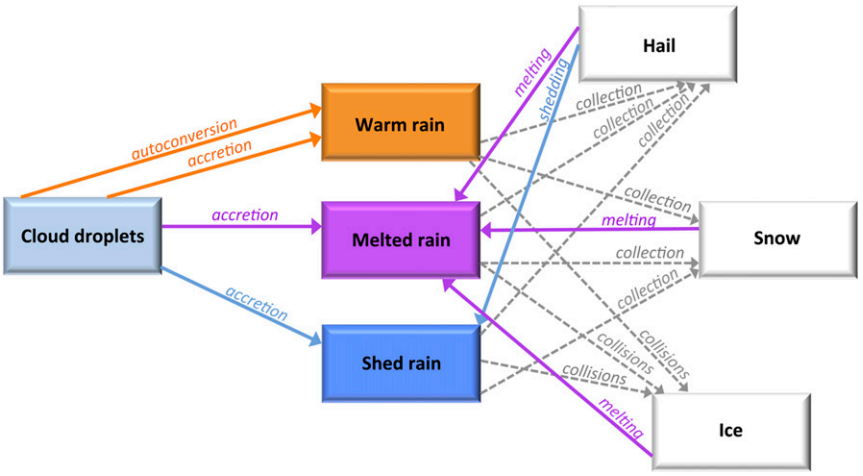

FIG. 1. Schematic illustrating the microphysical processes that affect the different rain classes. Source terms for the rain classes are shown in color-coded solid arrows, whereas sinks are shown as dashed gray arrows. See text for more details.

selected for the rimed ice, with the particle density equal to 900 kg m^{-3} and fall speeds comparable to those of hail. Details of the process rate calculations and source and sink terms for each of the hydrometeor species can be found in Morrison et al. (2005) and Morrison et al. (2009).

The Morrison microphysics scheme has been modified (herein "RainClass") such that it now has three categories of rain representing the different mechanisms by which raindrops are produced: warm rain, shed rain, and melted rain. Each rain class is fully two moment in that the mass and number mixing ratios are prognosed. The original formulations for sedimentation, advection, and diffusion are identical to those described in Morrison et al. (2009), and are applied to each rain class. Conservation equations for the mass (q) and number (N_T) mixing ratios are given as follows:

$$\frac{\partial q}{\partial t} = -\mathbf{v}\cdot\nabla q + \frac{1}{\rho_{\text{air}}}\frac{\partial(\rho_{\text{air}} V_{qx} q)}{\partial z} + \Delta_D q + \left(\frac{\partial q}{\partial t}\right)_{\text{process}}, \tag{1}$$

$$\frac{\partial N_T}{\partial t} = -\mathbf{v}\cdot\nabla N_T + \frac{1}{\rho_{\text{air}}}\frac{\partial(\rho_{\text{air}} V_{Nx} N_T)}{\partial z} + \Delta_D N_T + \left(\frac{\partial N_T}{\partial t}\right)_{\text{process}}, \tag{2}$$

where the first three terms on the right-hand side are advection by the three-dimensional wind vector $\mathbf{v}$, sedimentation (with mass- and number-weighted fall speeds V_{qx} and V_{Nx}, respectively, and where ρ_{air} is the air density), and diffusion. The time rate of change of the mixing ratios due to various microphysical processes are grouped into the final term. The schematic in Fig. 1 illustrates important microphysical processes affecting the rain classes and how mass is distributed from one class to another. The main source terms for warm-rain mass are autoconversion of cloud liquid droplets and accretion of cloud droplets by warm-rain drops. Warm-rain mass is lost to water vapor by evaporation and lost to snow and hail via collection by those ice particles. Additionally, collisions between warm-rain drops and ice crystals can lead to mass lost to the snow or hail categories, depending on the warm-rain mass mixing ratio.

Melted rain originates from the melting of hail, snow, and cloud ice. Additional mass is added to the category by accretion of cloud liquid drops onto melted-rain drops. Melted-rain mass is lost via evaporation to water vapor, collection by hail and snow, and collisions with ice crystals that lead to a transfer of the mass to hail or snow. Shed rain is produced when hailstones collect rain mass at temperatures >273.15 K. This collected mass is immediately shed as 1-mm-sized drops. Additional mass is gained by accretion of cloud droplets onto shed-rain drops. Similar to the other classes, shed-rain mass is lost by evaporation, collection, and collisions with ice.

When any rain category is collected by hail at temperatures >273.15 K, the mass of this water is immediately shed as 1-mm drops and placed in the "shed" drops category. Thus, melting hailstones can "process" other rain classes and transfer them to the shed category. This is important because drops initially larger than 1 mm that are collected by hailstones will be shed as

smaller 1-mm-sized drops, fundamentally affecting the resulting rain DSD and evaporation and sedimentation rates. Shedding during wet growth at subfreezing temperatures is neglected, as it is not a process included in the Morrison microphysics scheme.

Aside from the typical uncertainties or caveats present in the two-moment Morrison scheme, it is worth mentioning that the different rain classes do not interact with each other. Though each class may be collected by snow and hail, and self-collection within a class is also accounted for, there is no collection among different rain classes. Effectively, this means that *part* of rain collection is turned off. This is because there is no simple solution to treating collisions between different rain classes while still retaining the information about the origin of the raindrops. Note, however, that rain mass is still conserved, and collisions between different rain classes would not change the proportion of total rain mass originating from the different mechanisms, only the number concentration. As we demonstrate below, neglecting such interactions does not substantially alter the behavior of the simulated storm.

b. Simulation design

An idealized supercell was simulated using both of the aforementioned microphysical schemes in the Weather Research and Forecasting (WRF) Model version 3.4.1 (Skamarock et al. 2008). The model domain encompassed 150 km in both horizontal directions and 24 km in the vertical. The horizontal grid spacing was set to 200 m, while a slightly smaller grid spacing of approximately[1] 120 m was used in the vertical (corresponding to 200 levels). Numerical simulations have suggested that grid lengths on the order of 100–200 m are necessary so that traditional large-eddy simulation subgrid closures perform according to their design by resolving part of the inertial subrange (e.g., Bryan et al. 2003; Bryan and Morrison 2012). The model was integrated for 3 h with a dynamical time step of 1.5 s to ensure numerical stability. Furthermore, a 5-km dampening layer was imposed at the model top. Horizontal advection and vertical advection were computed using the fifth- and third-order positive-definite advection schemes, respectively. The boundaries were open in both the x and y directions; the model top was a rigid lid. Radiation and surface fluxes were neglected in this study. This is not to say they are unimportant. In fact, Frame and Markowski (2013) showed that radiative effects owing to anvil shadowing can enhance low-level shear in anvil-shaded regions as vertical mixing of momentum is shut off in their simulations. Moreover, Schenkman et al. (2012, 2014) found that surface friction played a significant role in tornadogenesis in their high-resolution full-physics simulations. However, in order to focus the analysis on only the partitioning of rain via its formation mechanisms and to simplify the simulations, these processes are neglected. This is in accord with the vast majority of studies utilizing idealized supercell simulations.

The model was initialized with the Weisman and Klemp (1982) sounding, which has a most unstable convective available potential energy (MUCAPE) of approximately 2700 J kg^{-1}. The shear profile follows the idealized ''quarter-circle hodograph'' of Weisman and Rotunno (2000) that comes standard in the WRF package. To initiate convection, a thermal bubble was applied at the surface with a horizontal radius of 10 km and a vertical radius of 1.5 km. The maximum temperature perturbation was 3 K, decreasing following a cosine function outward from the center. This initialization is similar to that used in Morrison and Milbrandt (2011).

3. Comparison with the Control run

Before exploring the rain physics in our idealized supercell simulation, we must first ensure that the modified microphysics scheme has not fundamentally altered the simulated storm. Such a comparison of different storm attributes allows us to assess whether the two simulated storms exhibit substantially different behavior and evolution. Figure 2 provides snapshots of the reflectivity factor at horizontal polarization Z_H field at the lowest grid level every 30 min from t = 1–3 h for the Control and RainClass simulations. The general evolution of the dominant right- and left-moving supercells is remarkably similar over the simulation time, whereas some differences are noted in the smaller convective cells forming between them. However, even after three hours of simulation time, the dominant right-moving supercell is in very nearly the same location and has a similar structure in both the Control and RainClass simulations. This indicates that the supercells are propagating at very nearly the same speed and direction and that the overall structure and evolution of the storms are not appreciably different. Given the much larger differences in simulated squall-line propagation speeds owing to slight modifications to the raindrop breakup scheme presented by Morrison et al. (2012), the similar storm behavior in the Control and RainClass simulations is a strong indication that the RainClass microphysics scheme modifications do not fundamentally alter the bulk behavior of the storm.

[1] The vertical grid was slightly stretched to provide higher resolution at low levels such that the minimum grid spacing is ~100 m and the maximum grid spacing at the top of the domain is ~200 m.

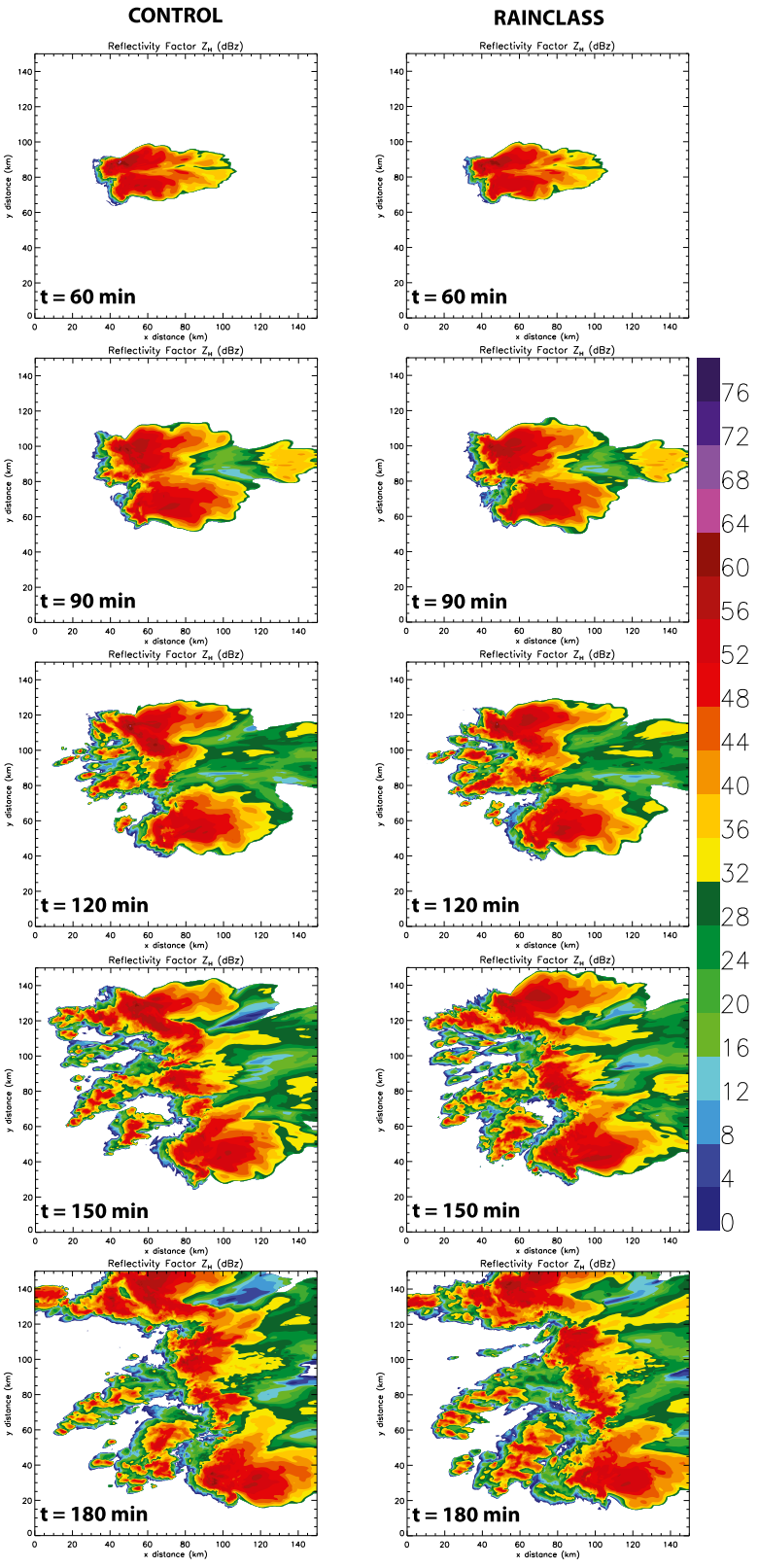

FIG. 2. Evolution of the Z_H field at the lowest model grid level (shaded according to scale in dBz) for the (left) Control run and (right) RainClass simulation every 30 min from $t = 60$ to $t = 180$ min.

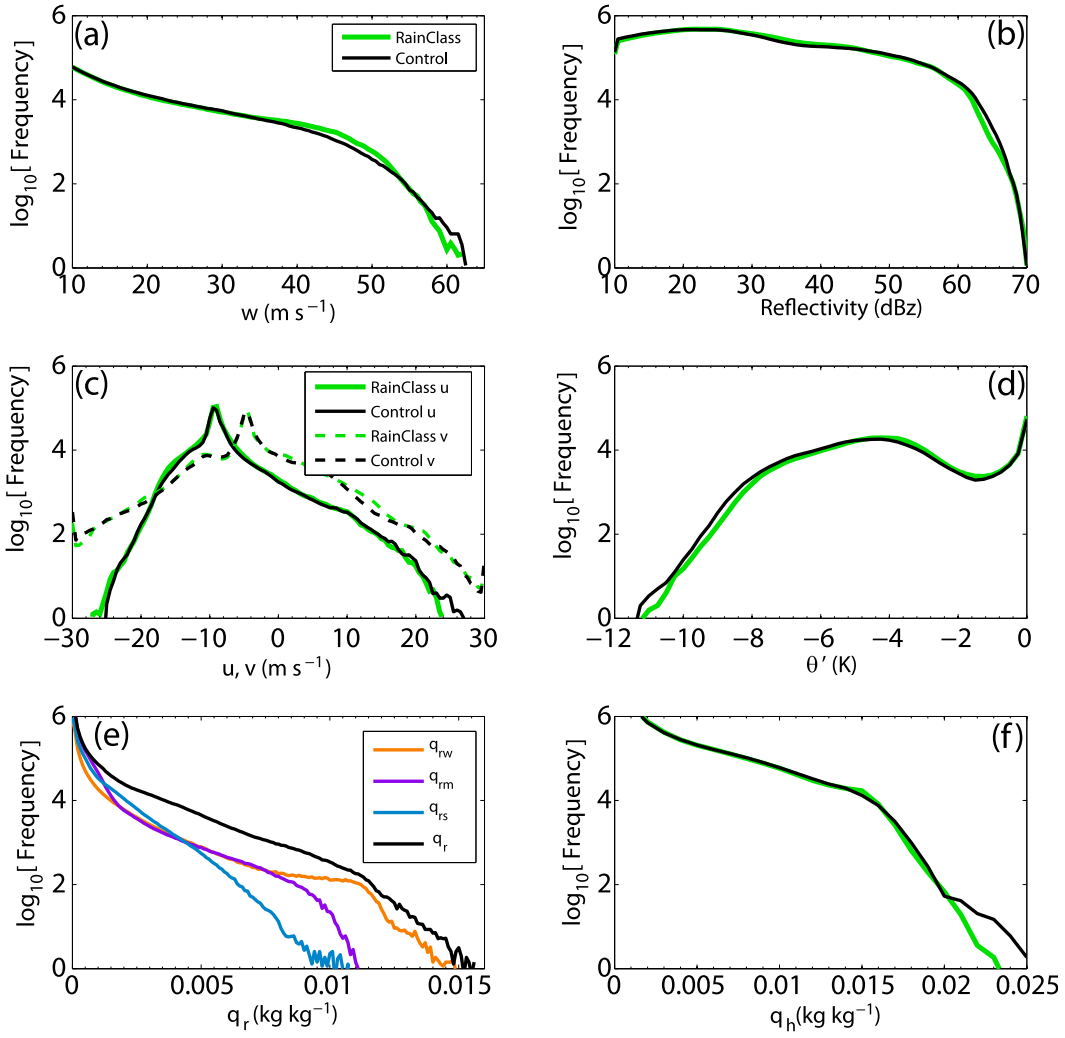

FIG. 3. Comparison of frequency distributions of meteorological quantities of interest for the Control run (black) and modified RainClass simulations (green): (a) updraft velocity, (b) simulated Z_H, (c) horizontal (u and v) wind speeds (solid and dashed, respectively), (d) potential temperature deficits at the lowest grid level, (e) rain mass mixing ratios, and (f) hail mass mixing ratio. In (e), each of the rain classes are shown (warm rain in orange, melted rain in purple, shed rain in blue, and total rain mass in black). The logarithm of frequency is shown on the ordinate axes. The frequency distributions were calculated over the last hour of the simulation.

To compare the simulations more quantitatively, we construct frequency distributions of meteorological quantities of interest from the Control and RainClass runs (Fig. 3). The distributions were constructed for the entire domain by counting grid boxes at each output time (10 min) falling within certain intervals of the variable of interest (e.g., 0.5 m s^{-1} for velocities, 0.5 dBz for reflectivity, etc.), and averaged over the last hour of simulation time (t = 2–3 h). Distributions of updraft speeds (Fig. 3a) between the two simulations are very similar. There is a slightly larger frequency of 35–50 m s^{-1} updrafts for the RainClass simulation, whereas the Control run features slightly more updrafts >55 m s^{-1}. Downdraft speeds are qualitatively similar (not shown). Likewise, Z_H distributions (Fig. 3b) are identical except for slightly more frequent occurrences of 60–65-dBz grid boxes in the Control run. The horizontal wind speeds (Fig. 3c) show only subtle differences, with an indication of slightly stronger westerlies in the Control run. The most extreme potential temperature deficits are somewhat larger in the Control run, though the distributions are virtually identical for $\theta' > -7$°C (Fig. 3d). The rain mass mixing ratio distributions are qualitatively similar (Fig. 3e). In the RainClass simulation, the maximum values of warm-rain mass mixing ratio are largest, followed by melted rain

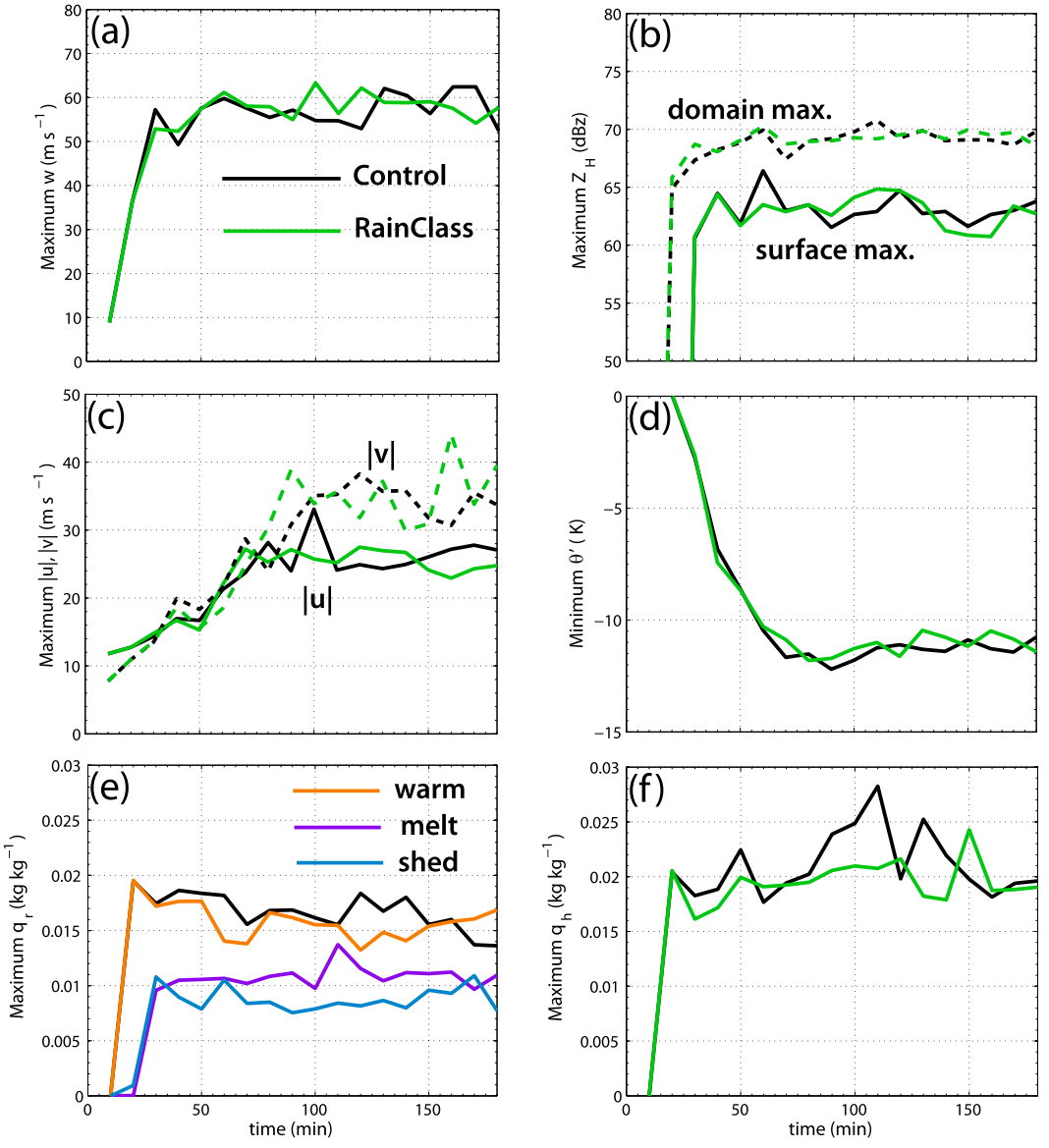

FIG. 4. Time series comparing various quantities between the Control (black curves) and modified microphysics simulations (colored lines). (a) Domain maximum updraft velocity w (m s^{-1}); (b) surface (solid) and domain (dashed) maximum reflectivity factor Z_H (dBz); (c) surface maximum wind speed magnitude of the u (solid) and v (dashed) components; (d) surface minimum potential temperature perturbation θ' (°C); (e) domain maximum rain mass mixing ratio q_r (kg kg^{-1}), with warm rain in orange, melted rain in purple, shed rain in blue, and black is the Control run; and (f) domain maximum hail mass mixing ratio q_h (kg kg^{-1}).

and shed rain. Finally, the hail mass mixing ratio distributions are nearly identical between the two simulations up to approximately 0.02 kg kg^{-1}, above which there are more frequent occurrences of large hail mass mixing ratios for the Control run (Fig. 3e).

Because most of the differences in the two simulations occur for extreme values, time series of extrema of the same quantities are presented in Fig. 4. Both simulations develop storms with persistent strong (~60 m s^{-1}) updrafts (Fig. 4a). Similarly, the domain maximum and surface maximum Z_H (Fig. 4b) are quite similar throughout the 3-h simulation. Aside from the timing of occasional wind speed surges, the maximum magnitudes of both horizontal components of the surface wind (Fig. 4c) exhibit similar patterns, including having larger magnitudes in the north–south direction than in the east–west direction. The minimum surface potential temperature perturbation (Fig. 4d) remains within

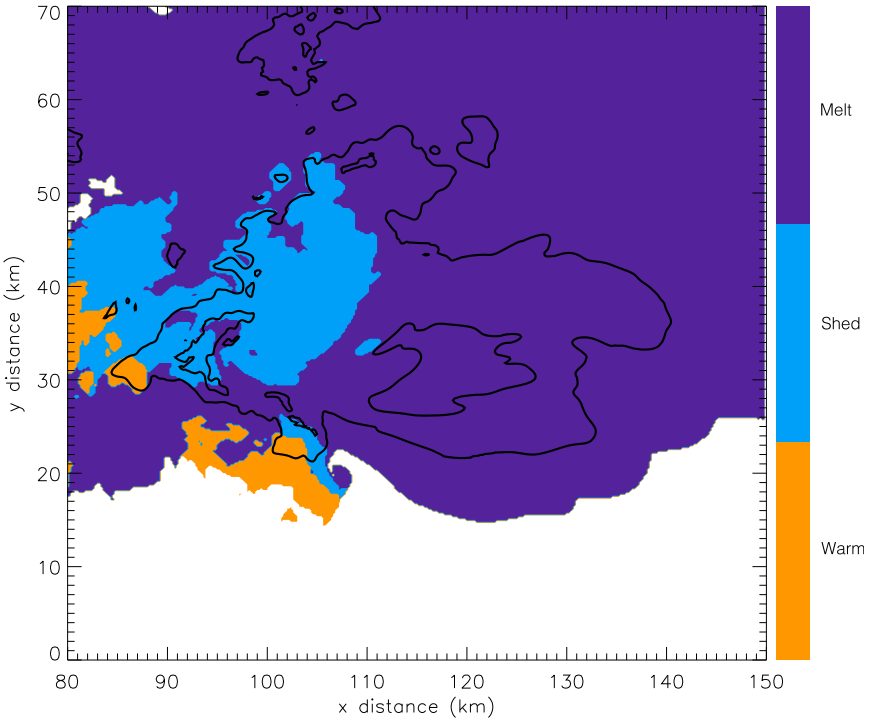

FIG. 5. Mass dominant rain class at the lowest grid level at $t = 180$ min. Purple shows melted rain, blue is shed rain, and orange is warm rain. The Z_H contours of 35, 45, and 55 dBz at the lowest grid level are overlaid.

approximately 1°C between the simulations at all times. Warm rain exhibits the largest domain maxima, just under that of the Control run for most output times (Fig. 4e). A noteworthy difference is the maximum hail mass mixing ratio, which is slightly less in the RainClass simulation than the Control run (Fig. 4f), particularly after 1 h into the simulation.

Overall, the distribution and behavior of these quantities throughout the duration of the simulations are quantitatively similar, as is the appearance of the evolution of the simulated Z_H field. This result strongly suggests that the simulated storms are quite similar and that the modified microphysical scheme did not substantially alter the behavior or evolution of the simulated supercell. Other studies (e.g., Morrison and Milbrandt 2011; Morrison et al. 2012) have demonstrated far more significant structural or behavioral changes in simulated convective storms when comparing different two-moment schemes, and *even different parameter settings within the same scheme*. Thus, we argue that direct comparisons between our two runs are warranted. Furthermore, the use of the RainClass scheme does not fundamentally alter the fact that the simulation still produces a supercell storm; therefore, we can use the model as a tool to investigate the rain microphysics in this simulated supercell.

4. Analysis of rain partitioning results

To explore the relative importance of each class of rain in various parts of the storm, we determine the class with the dominant mass mixing ratio at each grid box. An example from the lowest grid level at $t = 180$ min is shown in Fig. 5. Much of the forward flank is dominated by rain arising from melting hail. However, the left flank of the storm has a large area dominated by drops shed from wet hailstones. The importance of shedding for particles in the left flank of the supercell is in good accord with hail growth and trajectory calculations of Miller et al. (1988) in their study of a northern plains supercell. All three rain types are dominant in various parts of the hook echo, including melted drops in the inflow side, shed drops in the middle, and warm rain at the back. The only place warm rain is dominant at low levels is in the rear of the storm. The warm rain is generated in small-scale updrafts associated with a loosely organized band of convergence that runs southeast to northwest along the rear edge of the Z_H echo and slopes toward the northeast with increasing height (Fig. 6).

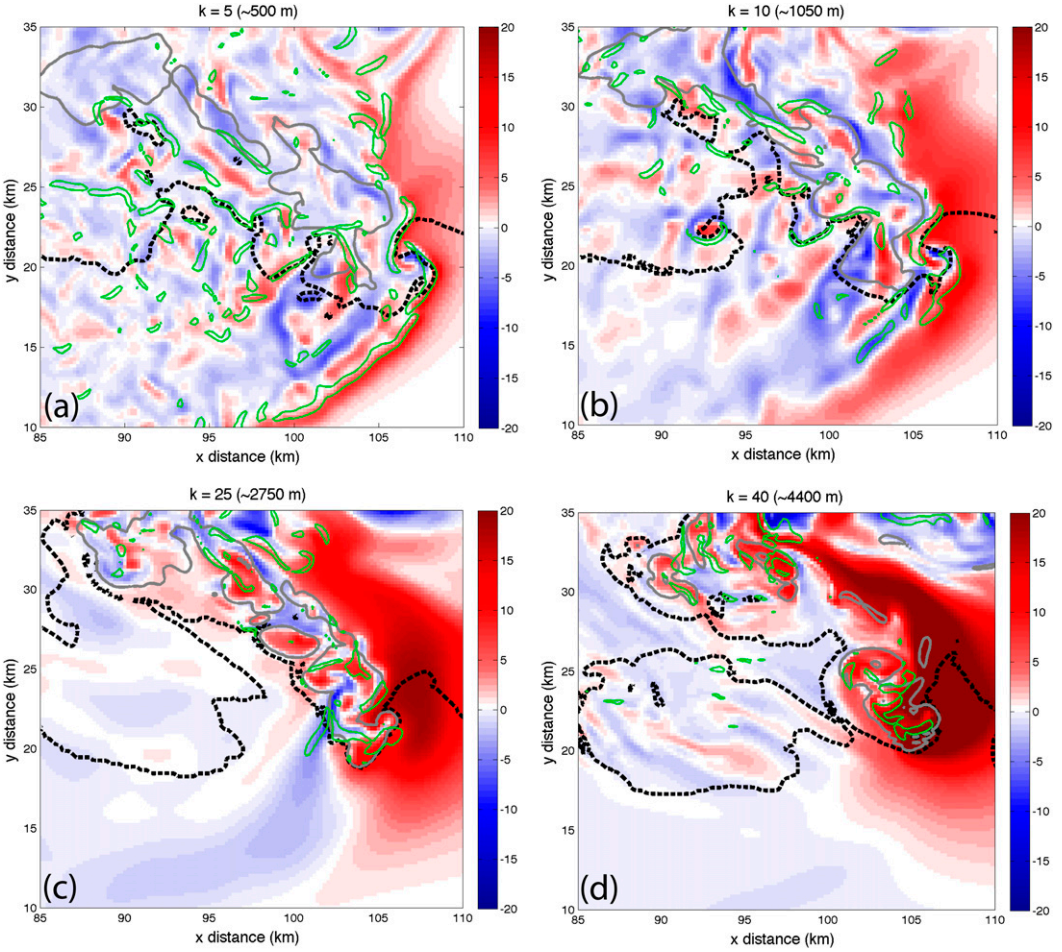

FIG. 6. Horizontal cross sections at four different heights from $t = 180$ min into the simulation: about (a) 500, (b) 1050, (c) 2750, and (d) 4400 m AGL. Updrafts and downdrafts are shaded according to the color scale. Overlaid are the 0-dBz contours of Z_H (black dashed lines), convergence ($0.01\ s^{-1}$, contoured in green), and the $0.1\ g\ kg^{-1}$ mixing ratio of warm rain in gray.

Such a feature is also apparent in recent numerical simulations by Beck and Weiss (2013), Markowski and Richardson (2014), Markowski et al. (2014), and A. Schenkman (2015, personal communication). Additionally, observational analyses by Kosiba et al. (2013) and Y. Richardson (2015, personal communication) have revealed convergence and/or small updrafts in the rear of the Goshen County, Wyoming, supercell storm during VORTEX2 (Wurman et al. 2012). This band of convergence occurs between southerly and southwesterly momentum overrunning the rear-flank outflow and northerly and northeasterly momentum from the forward-flank outflow and is distinct from the main updraft region associated with the primary rear-flank gust front, which is visible in Fig. 6a (running from about $x = 100$, $y = 10$ km to about $x = 108$, $y = 20$ km). Warm rain is generated in these small-scale updrafts (most evident in Fig. 6c). Many of these updrafts do not connect with the main updraft, instead being confined to low and midlevels. In fact, some of these updrafts and their associated warm-rain mixing ratio contours entirely disappear from view above 4 km AGL (Fig. 6d). In contrast, the largest warm-rain mass mixing ratio values below 0.5–1 km AGL are found within downdrafts (Figs. 6a,b). This strongly suggests that the warm rain at the lowest levels is generated in smaller-scale low-level updrafts, whereupon it sediments and/or is transported to the surface in low-level downdrafts. This structure is consistent throughout the simulation and is in generally good agreement with suggestions of Kumjian (2011).

The mass mixing ratio of warm rain at the lowest model level is shown in Fig. 7. Note that appreciable warm-rain mass (only grid points with $>1.0 \times 10^{-5}\ g\ kg^{-1}$ are shaded) is found only in the rear of the storm;

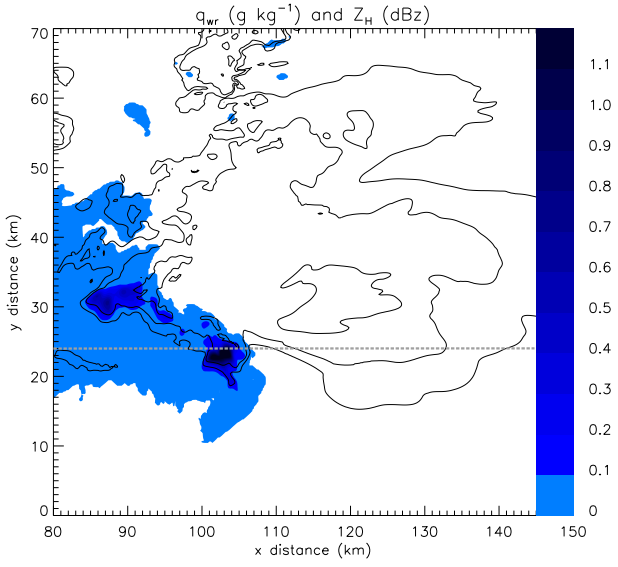

FIG. 7. Rain mass mixing ratio for warm rain (q_{rw}) shaded according to scale in g kg^{-1} at $t = 180$ min into the simulation at the lowest model level. Overlaid are Z_H contours of 35, 45, and 55 dBz at the lowest grid level.

the majority of the rain in the rest of the storm comprises melted and shed drops. Of note is the small area of enhanced warm-rain mixing ratio in the rear of the hook echo, with maximum values near 1.7 g kg^{-1}. Warm rain was found within a similar location of a simulated supercell by Van Den Broeke (2014), who used an idealized half-circle hodograph for the environmental wind profile. Van Den Broeke (2014) ran several simulations using differing thermodynamic profiles and found that the maximum low-level warm-rain mass mixing ratio (averaged over 70 min) varied by up to 25%. However, the qualitative structure of the warm-rain field remained the same across the different simulations.

To explore the origin of warm rain in the rear of the storm, selected three-dimensional isosurfaces are constructed. An example of one is shown in Fig. 8. This view reveals turrets of warm-rain mass mixing ratio (the 0.6 g kg^{-1} isosurface is shown) confined mainly to low levels in the rear of the storm, consistent with the expected growth processes of warm rain. The notable exception is the vertically extensive region of warm-rain mass associated with the storm's main updraft. The only region where this particular isosurface reaches the ground is in the "bull's-eye" of enhanced values seen in Fig. 7. Also included in Fig. 8 are the downdraft $w = -7$ m s^{-1} isosurfaces (in gray). The only region in the domain where the w isosurfaces approach the ground is in the vicinity of the hook echo, where small-scale dynamically forced downdrafts are expected (e.g., Klemp and Rotunno 1983; Markowski 2002, and

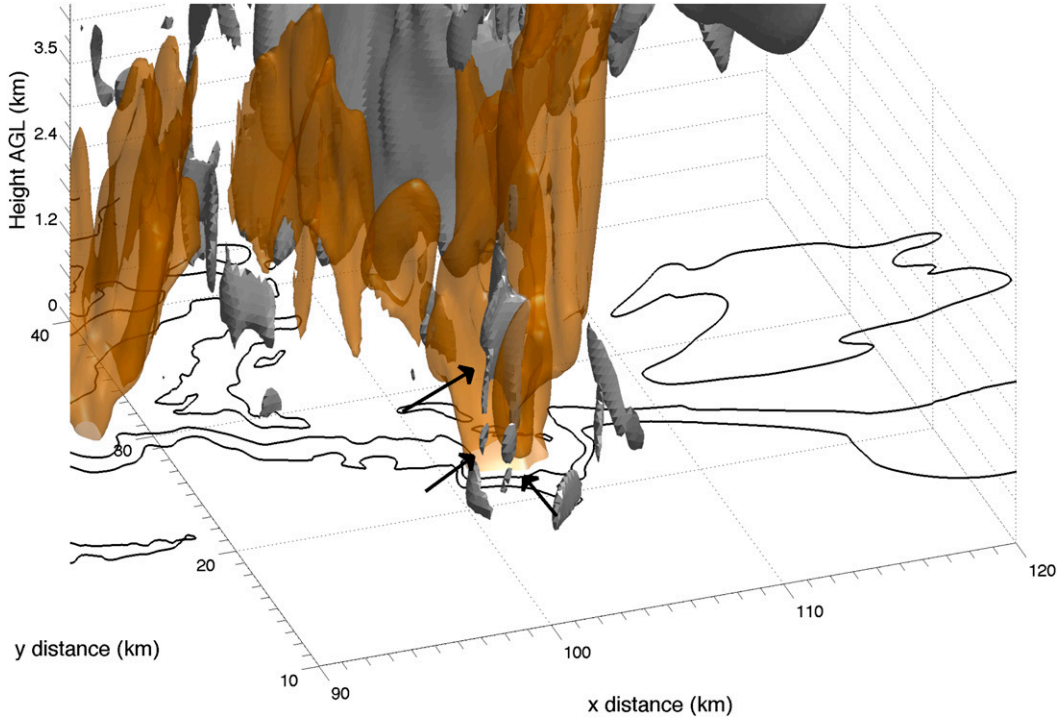

FIG. 8. Three-dimensional downdraft (gray) and warm-rain (orange) isosurfaces of 7 m s^{-1} and 0.6 g kg^{-1}, respectively, at $t = 180$ min; the lowest grid-level contours of Z_H (35, 45, and 55 dBz) are underlaid. The arrows point out small-scale downdrafts near the hook echo.

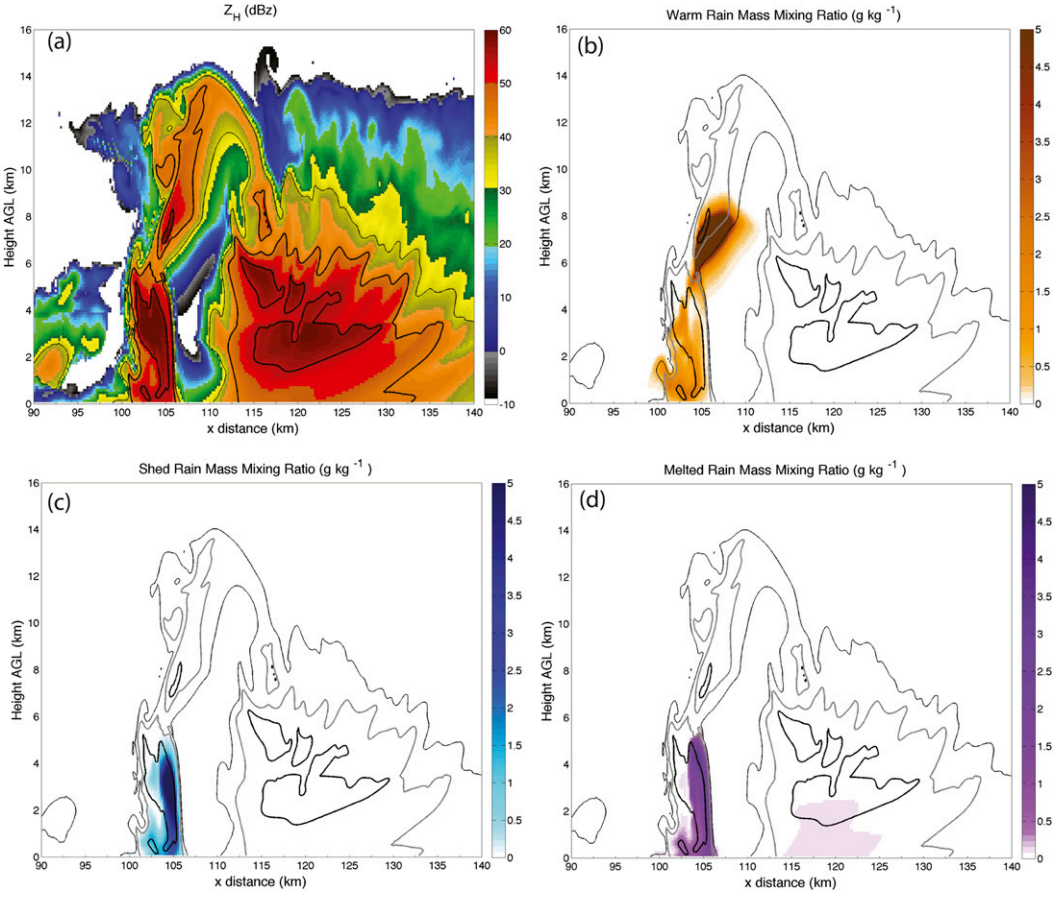

FIG. 9. Vertical cross sections through the supercell at $t = 3$ h into the simulation, along $y = 24$ km. (a) Simulated Z_H (dBz), (b) warm-rain mass mixing ratio q_{rw} (g kg^{-1}), (c) shed-rain mass mixing ratio q_{rs} (g kg^{-1}), and (d) melted-rain mass mixing ratio q_{rm} (g kg^{-1}). In each panel, 35-, 45-, and 55-dBz contours of Z_H are overlaid. In (b)–(d), the Z_H contours are thin black, thick gray, and thick black for 35, 45, and 55 dBz, respectively.

references therein). Indeed, the shaft of enhanced warm-rain mass mixing ratio is collocated with one of these enhanced downdrafts, seemingly consistent with the hypothesis put forth in Kumjian (2011).

A vertical cross section (Fig. 9) is taken through the hook echo, main updraft, and inflow edge of the forward flank, as indicated by the gray dashed line in Fig. 7. The Z_H structure in Fig. 9a displays a prominent bounded weak echo region (BWER) extending to more than 10 km above the surface. Warm-rain mass is found not only in the hook echo at low levels but also aloft in the main updraft (Fig. 9b). In fact, the largest shed-rain mass mixing ratios (hereafter q_{rw}) are aloft, where vigorous updrafts lead to strong adiabatic cooling and large condensation rates. This also explains why the domain-maximum q_{rw} is the largest of the three classes in Fig. 4. In contrast, the shed- and melted-rain mass mixing ratios reach heights of only ~5 km (Figs. 9c,d), reflecting the fact that shedding and melting only occur at temperatures >0°C. For these simulations, the environmental 0°C level is at ~3.7 km AGL, though within the storm the 0°C level ranges from about 3.3 to 4.8 km AGL. The vertical extent of shed and melted rain above 3.7 km thus indicates a local upward perturbation of the 0°C level by the updraft. The shed- and melted-rain maxima are found on the front side of the hook echo, at the periphery of the BWER. The q_{rm} and q_{rs} regions are heavily overlapped, though the q_{rm} maximum occurs above and to the right (front side of the hook echo and closer to the BWER) of the q_{rs} maximum. This arrangement makes sense because only after sufficient liquid water is present from melting or collection of warm or melted rain can hailstones shed this mass. A secondary area of q_{rm} is found at low levels within the highest Z_H in the forward flank, indicative of mass produced by melting ice particles. Because of the location of the cross section relative to the storm's forward flank (cf. Fig. 7), these q_{rm} values are quite small.

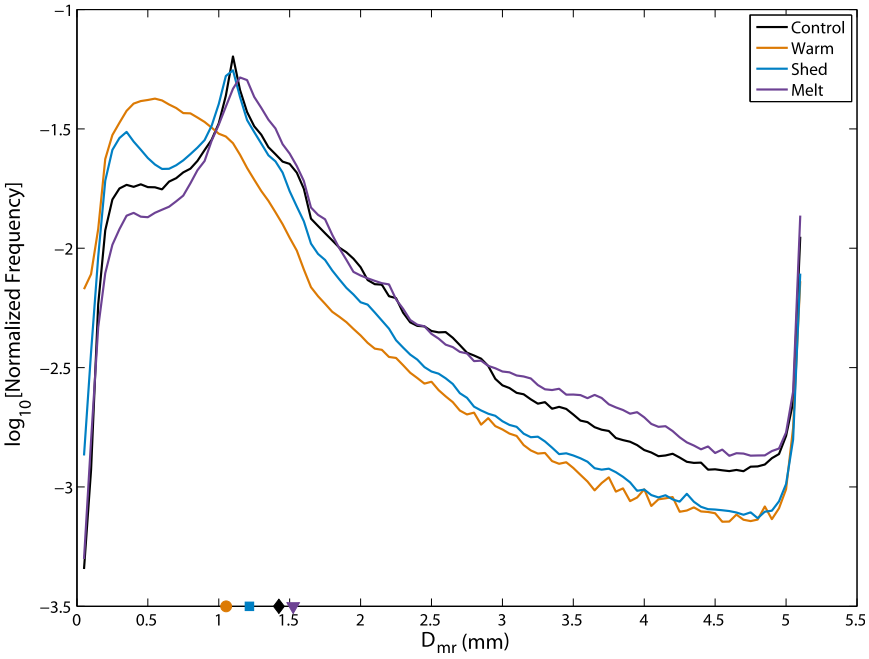

FIG. 10. Normalized frequency distribution of the mean–mass diameter (D_{mr}) of raindrops for the Control run (black) and the modified microphysics rain classes: warm rain (orange), melted rain (purple), and shed rain (blue). The mean D_{mr} for each category is indicated by the colored markers on the abscissa. The frequency distributions were averaged over the last hour of the simulation at the lowest grid level.

The mean–mass diameter of raindrops (D_{mr}) combines both prognostic moments to provide a characteristic drop size of a given simulated DSD. Normalized frequency distributions of D_{mr} averaged over the last hour of the simulation for the Control and RainClass simulations at the lowest grid level are shown in Fig. 10. The warm-rain category is characterized by the smallest average drop size (average mean–mass diameter of warm-rain drops $\overline{D}_{mrw} = 1.05$ mm), exhibiting a much larger relative proportion of small (<1 mm) D_{mr} rain than the other categories. Warm rain also has a lower frequency of D_{mr} values >1.0 mm than the other categories. In contrast, melted-rain drops have the largest average mean–mass diameter ($\overline{D}_{mrm} = 1.52$ mm), featuring proportionally less D_{mr} values <1.0 mm than warm and shed rain and a much higher relative frequency of $D_{mr} > 1.0$ mm than the other categories. Shed-rain drops have an intermediate average D_{mr} value ($\overline{D}_{mrs} = 1.22$ mm), exhibiting a bimodal frequency distribution with peaks near $D_{mr} = 1.10$ and 0.35 mm. In comparison, the normalized frequency distribution for the Control run generally follows that of melted rain, especially for $D_{mr} > 1.0$ mm. This is not surprising given that melted-rain mass dominates the total rain mass field at low levels in our simulation. The average $\overline{D}_{mr}$ for the Control run is 1.42 mm.

All categories have an abrupt increase in frequency for $D_{mr} \sim 5.1$ mm. This is representative of the largest D_{mr} allowed in the Morrison microphysics scheme; it is assumed implicitly that drop breakup does not allow larger D_{mr}. Such large mean–mass drop sizes occur as a result of size sorting. In multimoment bulk microphysics schemes, size sorting is emulated by having different fall speeds for each prognosed moment. In the case of a two-moment scheme like the one used in this study, the mass-weighted fall speed exceeds the number-weighted fall speed, allowing the mass mixing ratio field to sediment faster and thus be less affected by the storm-relative flow than the number mixing ratio field. Excessive size sorting occurs in two-moment schemes with a fixed exponential size distribution shape, like the model used here. Left unchecked, such overaggressive size sorting can lead to unrealistically large drop sizes (e.g., Wacker and Seifert 2001; Milbrandt and Yau 2005a; Milbrandt and McTaggart-Cowan 2010; Dawson et al. 2010; Mansell 2010; Kumjian and Ryzhkov 2012; Dawson et al. 2014). Thus, the scheme treats breakup explicitly by modifying the collection efficiency for rain self-collection and implicitly by providing a lower limit on slope parameter to prevent such overaggressive size sorting.

The mean–mass diameter of raindrops at the lowest grid level for each of the three rain classes is shown in

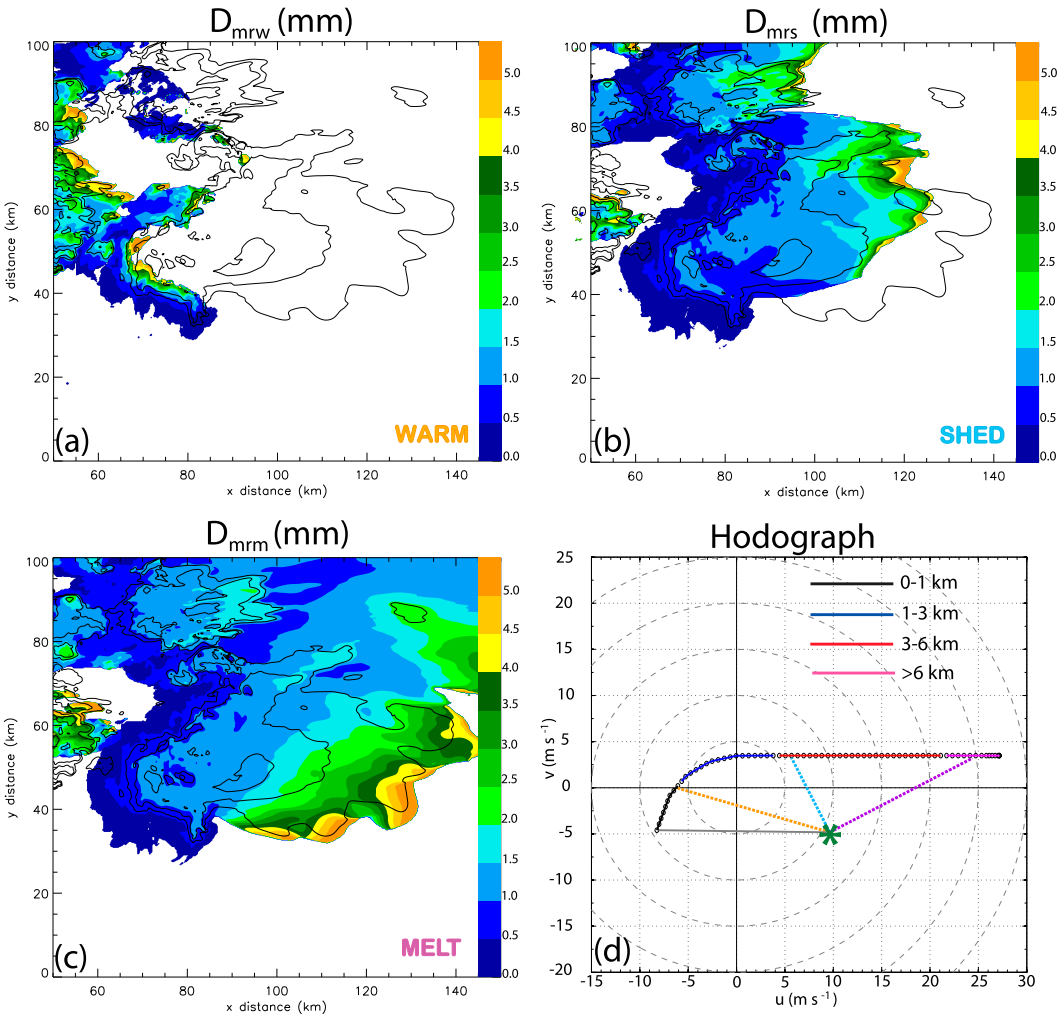

FIG. 11. Mean–mass diameter (mm, shaded according to scale) for each raindrop class at $t = 140$ min into the Control simulation. (a) Warm rain (D_{mrw}), (b) shed rain (D_{mrs}), and (c) melted rain (D_{mrm}). Overlaid are Z_H contours of 35, 45, and 55 dBz. (d) Hodograph for the simulation, with different layers marked by different colored lines (black for 0–1 km, blue for 1–3 km, red for 3–6 km, and magenta for >6 km). Also annotated is the estimated storm motion (green asterisk). The solid gray line shows the storm-relative flow at the lowest grid level. The dotted colored lines show the approximate top of the size-sorting layer for each of the rain categories (orange for warm, cyan for shed, and purple for melt). See text for details.

Fig. 11 at $t = 3$ h into the simulation. A characteristic D_{mr} gradient is observed in each rain category, with values >5 mm (i.e., the maximum value allowed) at the upstream or front of each rain mass field. This characteristic originates primarily because the precipitation encounters nonzero storm-relative flow over a layer as it descends (Fig. 11d) and thus undergoes size sorting, which leads to larger drop sizes at the upstream (in a storm-relative sense) edge of the precipitation shaft, whereas the smaller drops are advected farther downstream (e.g., see Kumjian and Ryzhkov 2012; Dawson et al. 2014, among others). This sorting effect leads to positively skewed raindrop size distributions. The effect of such size sorting is routinely observed in supercells using polarimetric radar measurements because the differential reflectivity Z_{DR} is related to the mean raindrop size. The so-called Z_{DR} arc (e.g., Kumjian and Ryzhkov 2008b, 2009; Dawson et al. 2014) signature along the inflow edge of the forward flank is routinely observed in supercells and is thought to be a manifestation of this process, leading to a sparse population of large raindrops.

The alignment of the Z_{DR} or D_{mr} gradient provides information about the average storm-relative winds in the overlying layer in which size sorting occurs (Kumjian and Ryzhkov 2009; Dawson et al. 2014,

2015). Thus, the different directions of the D_{mr} gradient for each of the rain classes indicate that the resulting rain distribution is affected by size sorting in layers of differing depths. The northeast–southwest-oriented D_{mr} gradient for warm rain in the main supercell's rear flank (Fig. 11a) suggests that the dominant size sorting occurs in the layer where the average storm-relative winds are northeasterly. For the idealized environmental hodograph used in these simulations (Fig. 11d), only easterly storm-relative winds are found at low levels. However, the actual storm-relative winds in the RFD have a much larger northerly component ($<-20\,m\,s^{-1}$, not shown) than in the ambient environment, which serves to rotate the direction of the mean storm-relative winds at low levels such that it better aligns with the observed D_{mr} gradient. Accounting for this enhanced northerly flow in the RFD, the apparent size sorting layer is in the lowest 1 km AGL, which reinforces the notion that the warm rain along the rear flank of the supercell is generated at low levels. In contrast, the more east–west orientation of the D_{mrs} gradient (Fig. 11b) implies that size sorting occurs within a layer with its top at 3 km AGL (Fig. 11d). Finally, the southeast–northwest D_{mrm} gradient (Fig. 11c) suggests the presence of size sorting in an even deeper layer, implying that the size sorting most important for the low-level distribution of raindrop sizes occurs aloft (i.e., when these hydrometeors are still hail), which is consistent with the findings of Dawson et al. (2014). These layers are annotated on the hodograph in Fig. 11d.

To facilitate comparison between radar observations and the simulated DSDs within the hook echo, we compute Z_H and Z_{DR} of rain-only points within the hook echo of the mature right-moving supercell at t = 3 h into the simulation. These points are compared to the "expected" Z_H–Z_{DR} relation found for rain in Oklahoma by Cao et al. (2008). This method of comparison is a simple way to explore and quantify how unusual a DSD is for a given Z_H, at least compared to continental deep convective storms (e.g., Kumjian 2011; French et al. 2015). Simulated DSDs were determined from the predicted mass and number mixing ratios. **T**-matrix calculations (e.g., Mishchenko 2000) were performed to obtain the scattering amplitudes of raindrops from 0.05 to 8.0 mm in equivalent volume diameter at S band at a temperature of 20°C [for details, see Kumjian and Ryzhkov (2012)]. Figure 12a shows the results from the Control run. A slightly positive bias in Z_{DR} compared to the Cao et al. (2008) relation for Oklahoma rain (overlaid green curve) is noted for rain $Z_H < 40$ dBz. For the highest Z_H, the points fall slightly below the expected relation, indicating somewhat smaller mean drop sizes than typically encountered in Oklahoma rain events. This finding may indicate insufficient generation of large drops via melting of hail (e.g., Ryzhkov et al. 2013) or overaggressive breakup of large drops (e.g., Kumjian and Prat 2014). Also of note is the lack of scatter present in these hook echo points, indicating little variability of the low-level DSDs.

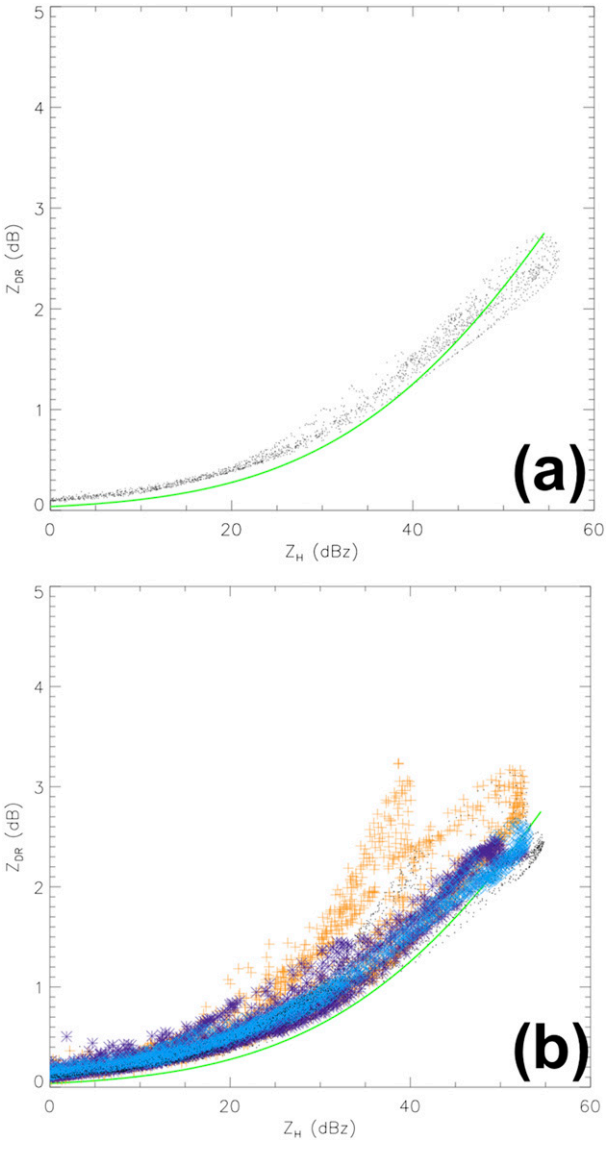

FIG. 12. Scatterplot of simulated Z_H vs Z_{DR} in rain (black dots) for (a) the Control run and (b) the modified RainClass run. Also in (b) are Z_H and Z_{DR} for each rain category in the colored markers: purple for melted rain, blue for shed rain, and orange for warm rain. Data are selected from the hook echo of the right-moving supercell at t = 180 min into the simulation. Overlaid on the plot is the expected relationship between Z_H and Z_{DR} derived from DSDs measured in Oklahoma by Cao et al. (2008) (green curve).

The Z_H–Z_{DR} scatterplot for the modified RainClass simulation is shown in Fig. 12b. The pattern is quite similar to the Control run; however, a few important differences are apparent. First, there is somewhat larger scatter, indicative of more diversity in the hook echo DSDs. When we separate the rain classes, a separation of the warm-rain points is seen for $Z_H > 30$ dBz. These points indicate much larger Z_{DR} (and thus much larger mean drop sizes) than expected for typical Oklahoma rain, which is consistent with positively skewed DSDs resulting from size sorting. Indeed, the fingerprint of size sorting of warm rain is observed within the hook echo and the supercell's rear flank (cf. Fig. 11a). This localized effect is distinct from the warm rain throughout the rest of the domain, which tends to exhibit smaller mean–mass sizes (cf. Fig. 10).

Of note is the lack of points substantially below the expected line, or points associated with DSDs heavily skewed toward small drops. As noted in the introduction, these types of DSDs have been observed in supercell hook echoes. One possible reason for this finding is that the model is unable to simulate these small-drop DSDs because of the way size sorting is handled in a two-moment scheme with a fixed spectral shape parameter (in this case, the shape parameter is such that the DSD shape is exponential). Size sorting causes the simulated DSD slope and intercept parameter to decrease. In the case of an exponential DSD, the decrease in these parameters can lead to substantial concentrations of large drops, which strongly affect the simulated radar variables. Such DSDs with small slope parameter lead to large sensitivities in the calculations of the radar variables, in which a maximum raindrop diameter must be specified for the integration. To demonstrate this point, the Z_H–Z_{DR} scatterplot of Fig. 12b is reproduced; however, this time, the maximum diameter of raindrops[2] defining the integral over the distribution for warm rain is set to 4 mm (Fig. 13). The warm-rain points now fall substantially below the expected curve, more consistent with the observations. There is a physical rationale for the reduced D_{max} of the warm-rain drops as well: these drops originate in low-level updrafts via warm-rain processes and have insufficient time to grow by coalescence to larger sizes; therefore, drops as large as 8 mm are not expected to originate by this mechanism. Because the mean–mass

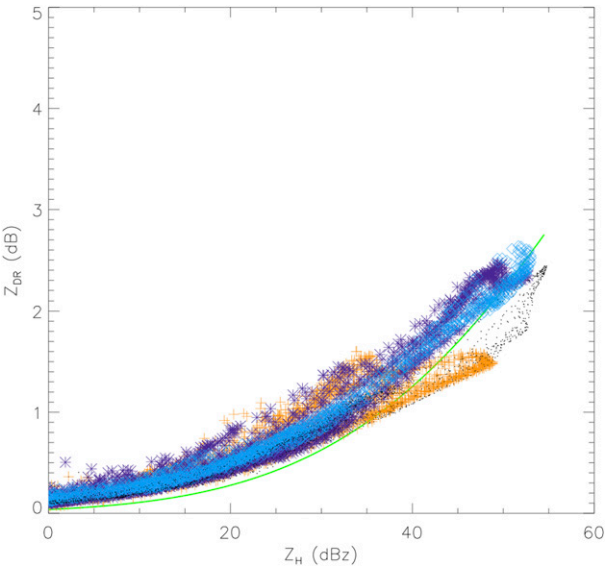

FIG. 13. As in Fig. 12b, but with $D_{max} = 4$ mm for warm rain.

drop size for shed and melted drops (D_{mrs} and D_{mrm}) is small throughout the hook echo, the impact of the maximum drop size in the Z_{DR} computations is not as large for these rain categories. This exercise reveals that comparisons of model output with observations require careful consideration of the limitations of the microphysics scheme.

The simulated DSDs across the hook echo at 3 h into the simulation are illustrated in Fig. 14. At both edges of the hook echo, the number of larger drops tapers off rapidly, which is also revealed in the tapering of the mass-weighted mean diameter $D_{4/3}$ (defined as the ratio of the fourth and third moments of the DSD) curve superimposed on Fig. 14. Other times (not shown) have similar DSD structures. Thus, the characteristic radar- and disdrometer-based observation of larger drops on the forward edge of the hook echo is not reproduced by this two-moment scheme. Furthermore, there is relatively little variability throughout the bulk of the wide hook, with Z_H, $D_{4/3}$, and the overall DSD shape changing very little. There is a noticeable maximum in $D_{4/3}$ at the rear edge of the hook. The DSDs from this portion of the hook are presented in more detail in Fig. 15, which shows the combined rain DSD as well as the DSDs of each rain class within the hook echo at 3 h into the simulation. The total DSD features a prominent "kink" in the total rain DSD at this point, which is indicative of contributions from multiple rain classes with different characteristic DSDs. Figure 15 indicates that shed and melted rain have similar DSDs with predominantly smaller drops, whereas the warm-rain DSD slope parameter decreases, contributing

[2] Incomplete gamma functions were used in the calculations because we assume a maximum raindrop size. Doing so introduces an inconsistency in the simulated DSDs compared to those used in process calculations in the microphysical code (where complete gamma functions were used). The example here is simply for illustrative purposes.

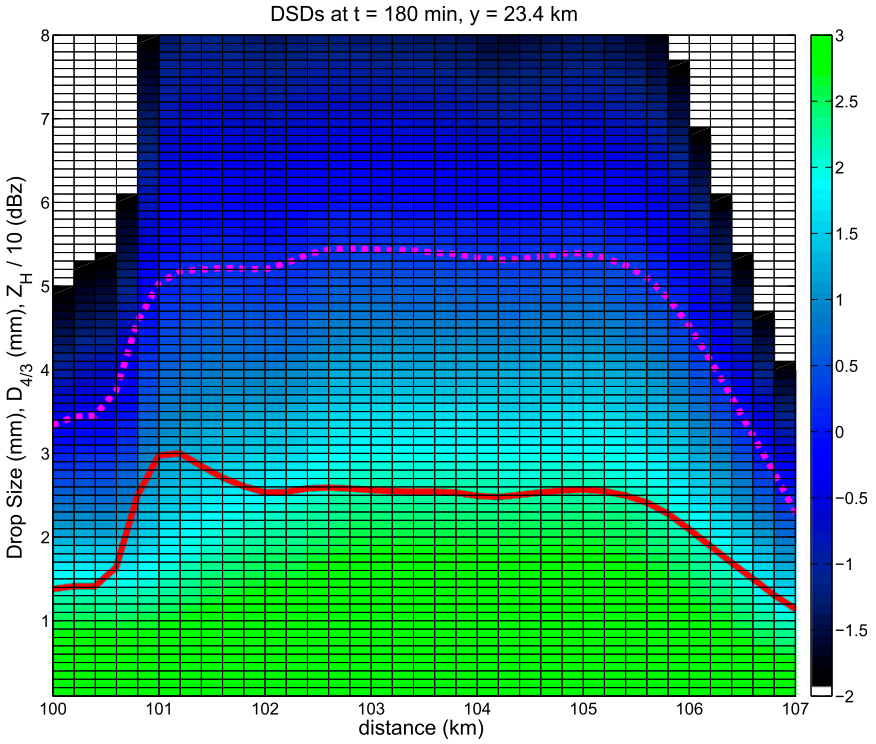

FIG. 14. Simulated surface DSDs (color shading) along a west–east track through the hook echo at $t = 180$ min and at $y = 23.4$ km (this is 0.6 km south of the line annotated in Fig. 7). The abscissa has the distance in the x direction, whereas the ordinate for the color shading is the drop size bin. The color scale refers to the base-10 logarithm of the raindrop number density $N(D)$ per size bin. Overlaid are the traces of mass-weighted mean diameter $D_{4/3}$ (red) and the total Z_H computed from all hydrometeor categories (dotted magenta, reduced by a factor of 10 to fit on the plot).

substantially to the drops >2 mm in diameter. The resulting total DSD is similar to a gamma distribution with a negative shape parameter or a biexponential distribution in appearance, which can arise owing to a mixture of two different hydrometeor populations (e.g., Ryzhkov et al. 2013).

Certain microphysical processes that shift warm-rain mass to larger sizes (e.g., self-collection and size sorting) lead to a reduction in the slope and intercept parameters of the warm-rain DSD, causing an artificial increase in the number of big drops. This finding suggests a disadvantage of using a fixed spectral shape parameter for two-moment schemes. Additionally, if the maximum drop size for warm rain were limited, the DSD would look substantially different; namely, a larger population of small drops owing to increased intercept and slope parameters. This underscores the necessity of limiting maximum drop size via treatment of breakup or other means of controlling excessive size sorting. Use of a prognosed third moment largely mitigates this problem by allowing the DSD to narrow during sedimentation and size sorting, eliminating the excessive large-drop end of the spectrum (e.g., Wacker and Seifert 2001; Milbrandt and Yau 2005a, among others).

5. Discussion

A caveat of the modified RainClass microphysics scheme is that collection between different rain categories is not accounted for. The self-collection of the jth category of raindrops depends on both the mass and number mixing ratios (q_{rj} and N_{Tj}, respectively), following Seifert and Beheng (2001):

$$\left.\frac{\partial N_T}{\partial t}\right|_{\text{coll}} = -5.78 N_{Tj} \times q_{rj} \times \rho_{\text{air}} \times E_{\text{cr}}, \qquad (3)$$

where ρ_{air} is the air density, E_{cr} is the collection efficiency between drops, and $(\partial N_T/\partial t)|_{\text{coll}}$ is the time rate of change of raindrop number mixing ratio due to self-collection. As mentioned in section 2a, the RainClass scheme accounts for self-collection of raindrops within each class, but not between classes. To investigate the potential impacts of neglecting part of rain coalescence, we can consider rain collection among two different classes as

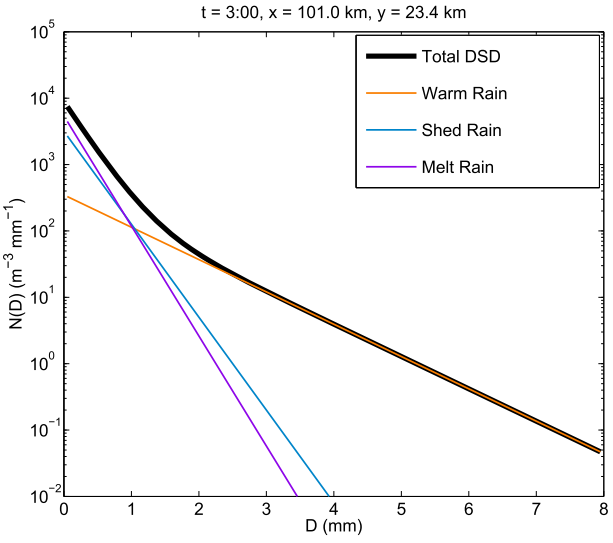

FIG. 15. Simulated surface DSDs at $t = 180$ min for $x = 101.0$ and $y = 23.4$ km. The total combined rain DSD is shown by the thick black curve, whereas the DSDs from each of the three rain classes are shown in thin colored curves (orange for warm rain, blue for shed rain, and purple for melted rain).

$$\left.\frac{\partial N_T}{\partial t}\right|_{\text{coll}} = -5.78 \times (N_{T1} q_{r1} + N_{T2} q_{r2} + N_{T1} q_{r2} + N_{T2} q_{r1}) \times \rho_{\text{air}} \times E_{\text{cr}}. \quad (4)$$

Thus, there are extra "cross terms" ($N_{T1}q_{r2}$ and $N_{T2}q_{r1}$) in the collection equation that are not accounted for in the RainClass scheme. Some of these cross terms are insignificant compared to the "co-terms". For example, the domain-average warm-rain co-term $q_{rw}N_{Tw}$ at $t = 3$ h into the simulation is 6.454, whereas the averages of the cross terms $q_{rw}N_{Tm}$ and $q_{rw}N_{Ts}$ are 0.0257 and 0.0791, respectively (the median of the co-term $q_{rw}N_{Tw}$ is also an order of magnitude larger than the cross terms). However, some of the cross terms are of the same order of magnitude: domain-averaged $q_{rs}N_{Tm} = 0.3408$ and $q_{rm}N_{Ts} = 0.3621$ compared to the domain-averaged shed-rain co-term $q_{rs}N_{Ts} = 0.5432$. Unlike the other cross terms, $q_{rs}N_{Tm}$ and $q_{rm}N_{Ts}$ occur with nearly the same frequency in the domain as the co-terms, which indicates substantial overlap between the melted and shed rain. Because of this overlap, neglecting the cross collection of these categories in some cases could lead to small errors in the *total* number of raindrops at these grid boxes (recall that the masses of each class are not directly affected by collection). The sign of the error depends on the mean drop size of the two categories undergoing collision. If the mean size of the two categories is near the equilibrium value for breakup and coalescence, then the "extra" collisions from the cross terms will not matter because they produce new drops by breakup. If the D_{mr} is larger than the equilibrium value, then neglecting the cross terms would lead to an overprediction of the mean drop size; the opposite would be true for D_{mr} less than the equilibrium value. The distribution of the overlapping points indicates that the majority occur when shed and melted rain have similar mean–mass diameters (not shown), in which errors are expected to be insignificant.

The aforementioned issues may affect evaporation and sedimentation rates (e.g., Dawson et al. 2010). However, we argue that these potential sources of error are relatively minor given the strong similarity of the cold pool and other storm characteristics between the Control and RainClass simulations. We also note that given the somewhat "arbitrary parameter settings" for raindrop collisional processes in two-moment schemes (Morrison et al. 2012), neglecting some of the rain coalescence and breakup should not introduce overwhelming uncertainties into our results.

Separation of rain classes based on the mechanism of their formation makes sense from a physical standpoint. Although the physical properties of raindrops (e.g., density and fall speeds) do not change among the different classes, the distribution of raindrop sizes arising from the different formation mechanisms can be dramatically different. Partitioning the classes allows for more variability in the overall rain DSD, or at least more than is possible using a single distribution function. On the other hand, such a partitioning for different ice species, at least from a physical standpoint, makes less sense. Typically, each class (e.g., cloud ice, snow, and graupel/hail) is prescribed vastly different physical properties, including fall speed, in order to capture the wide variability of ice particle properties. Having separate classes for ice hydrometeors thus requires the use of various thresholds for conversion from one class to another, whereas in nature, these ice particles evolve within a continuous spectrum. Often, these prescribed thresholds are "arbitrary" and not necessarily based on physics (Morrison and Milbrandt 2015). A new paradigm is emerging in which the physical properties themselves are predicted for a single hydrometeor class, allowing for more natural changes in particle characteristics (e.g., Hashino and Tripoli 2007; Harrington et al. 2013; Morrison and Milbrandt 2015). This approach is rooted in a physical basis and has the added benefit of being easier to validate with remote sensing or in situ observations, including dual-polarization radar observations.

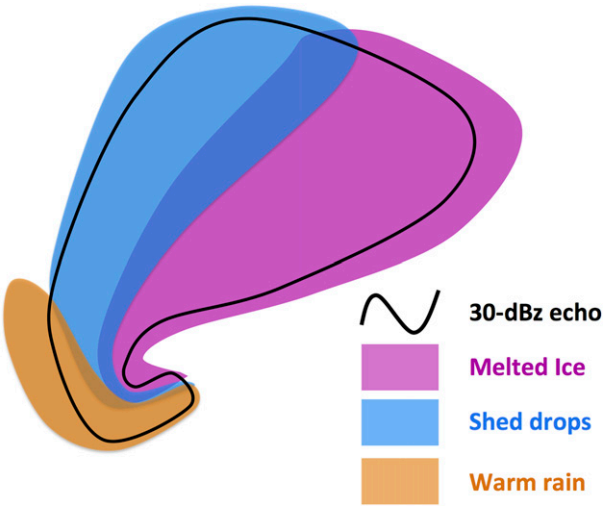

FIG. 16. Schematic summarizing the dominant source of raindrops at low levels in mature supercells based on the idealized simulation presented herein. The black outline indicates the approximate 30-dBz Z_H echo, and the purple, blue, and orange shading indicate where the rain mass is dominated by melted ice, shed drops, and warm-rain processes, respectively.

6. Summary

The Morrison microphysics scheme is modified to have three rain categories that are based on the mechanism of their origin (warm-rain processes, melting of ice, and shed from melting hailstones), following a similar technique employed by Van Den Broeke and Straka (2010) and Van Den Broeke (2014). Using this modified two-moment microphysics scheme, we have explored the generation sources of raindrops in an idealized supercell storm. Rain originating from melting ice dominates the precipitation field at low levels, especially along the right (relative to the storm motion vector) portion of the forward flank and far downstream of the updraft. In addition, rain from melting ice serves as the source of large drops along the inflow edge of the forward-flank precipitation echo, known as the Z_{DR} arc from polarimetric radar observations. Drops shed from melting hailstones are confined to the left portion of the forward-flank precipitation shield, which is overlapped with rain originating from melting ice. At low levels, rain generated by warm processes is confined to the rear of the storm, formed mainly in transient small-scale updrafts along the back edge of the Z_H echo. Figure 16 presents a schematic summarizing the dominant source region of raindrops at low levels in supercells based on the idealized simulation discussed herein. Aloft, warm-rain mass dominates in the updraft because cloud droplets are converted into raindrops due to the large amounts of condensate found there; supercell updrafts tend to be protected from the diluting effects of entrainment (e.g., Davies-Jones 1974; Lebo et al. 2012). These raindrops are subsequently lofted and eventually freeze.

Frequency distributions indicate that raindrops originating from warm-rain processes are, on average, smaller than those generated by shedding and melting, with melted-rain drops having the largest average mean–mass diameter D_{mr}. Analysis of D_{mr} of each rain category at low levels reveals patterns attributable to size sorting by storm-relative winds in different layers. Large D_{mr} values along the inflow edge of the forward-flank precipitation shield arise from size sorting and melting of ice hydrometeors, in agreement with Kumjian and Ryzhkov (2008b) and Dawson et al. (2014).

The appearance of warm rain in the rear of the storm is consistent with simulations by Van Den Broeke (2014) and agrees with the suggestions based on polarimetric radar observations by Kumjian (2011). The largest mass mixing ratios of warm rain appeared mainly within downdrafts in the lowest ~1 km AGL. This supports the intriguing possibility suggested by Kumjian (2011) and French et al. (2015) that the appearance of warm rain (manifested as small drops in polarimetric radar data) could be tied to momentum surges in the rear-flank downdraft. However, a much larger observational dataset and additional high-resolution simulations are needed to verify any relationship between the appearance of warm rain at low levels and RFD behavior and evolution.

Although the large-scale structure of raindrop sizes is reproduced in the simulations (including the large drops along the forward-flank precipitation echo observed as the Z_{DR} arc), the large heterogeneity in hook echoes observed in disdrometer and polarimetric radar observations is not. The two-moment framework (with fixed spectral shape parameter) used herein may be too rigid. This suggests that a more sophisticated treatment of the predicted DSD shape are required. For example, three-moment schemes or two-moment schemes with a diagnostic shape parameter (e.g., Milbrandt and Yau 2005a,b; Loftus et al. 2014; Dawson et al. 2014; Van Den Broeke 2014) that allow for physically based changes in the *shape* of the DSD are likely necessary to reproduce the varied DSD structure in supercell hook echoes.

Acknowledgments. Partial support for MRK for this work comes from Grant ER-65459 from the U.S. Department of Energy Atmospheric System Research program and from the National Center for Atmospheric Research Advanced Study Program. ZJL would like to thank NOAA's Climate Goal for funding. HCM was partially supported by U.S. DOE ASR SC0008468.

Professor Jerry Straka (University of Oklahoma) is thanked for useful discussions about his microphysics scheme over the years. We also acknowledge helpful discussions with Drs. Daniel T. Dawson and Alex Schenkman (CAPS/University of Oklahoma), Prof. Michael M. French (SUNY–Stony Brook), and Profs. Yvette Richardson and Paul Markowski (PSU). Prof. Matthew Van Den Broeke (University of Nebraska–Lincoln) and two anonymous reviewers are thanked for their valuable comments and criticisms, which significantly improved the clarity and presentation of the manuscript.

REFERENCES

Beck, J., and C. Weiss, 2013: An assessment of low-level baroclinity and vorticity within a simulated supercell. *Mon. Wea. Rev.,* **141,** 649–669, doi:10.1175/MWR-D-11-00115.1.

Bryan, G. H., and H. Morrison, 2012: Sensitivity of a simulated squall line to horizontal resolution and parameterization of microphysics. *Mon. Wea. Rev.,* **140,** 202–225, doi:10.1175/MWR-D-11-00046.1.

——, J. C. Wyngaard, and J. M. Fritsch, 2003: Resolution requirements for the simulation of deep moist convection. *Mon. Wea. Rev.,* **131,** 2394–2416, doi:10.1175/1520-0493(2003)131<2394:RRFTSO>2.0.CO;2.

Cao, Q., G. Zhang, E. A. Brandes, T. J. Schuur, A. V. Ryzhkov, and K. Ikeda, 2008: Analysis of video disdrometer and polarimetric radar data to characterize rain microphysics in Oklahoma. *J. Appl. Meteor. Climatol.,* **47,** 2238–2255, doi:10.1175/2008JAMC1732.1.

Davies-Jones, R. P., 1974: Discussion of measurements inside high-speed thunderstorm updrafts. *J. Appl. Meteor.,* **13,** 710–717, doi:10.1175/1520-0450(1974)013<0710:DOMIHS>2.0.CO;2.

Dawson, D. T., and G. S. Romine, 2010: A preliminary survey of DSD measurements collected during VORTEX2. *25th Conf. on Severe Local Storms,* Denver, CO, Amer. Meteor. Soc., 8A.4. [Available online at https://ams.confex.com/ams/pdfpapers/176115.pdf.]

——, M. Xue, J. A. Milbrandt, and M. K. Yau, 2010: Comparison of evaporation and cold pool development between single-moment and multimoment bulk microphysics schemes in idealized simulations of tornadic thunderstorms. *Mon. Wea. Rev.,* **138,** 1152–1171, doi:10.1175/2009MWR2956.1.

——, E. R. Mansell, Y. Jung, L. J. Wicker, M. R. Kumjian, and M. Xue, 2014: Low-level Z_{DR} signatures in supercell forward flanks: The role of size sorting and melting of hail. *J. Atmos. Sci.,* **71,** 276–299, doi:10.1175/JAS-D-13-0118.1.

——, ——, and M. R. Kumjian, 2015: Does wind shear cause hydrometeor size sorting? *J. Atmos. Sci.,* **72,** 340–348, doi:10.1175/JAS-D-14-0084.1.

Frame, J., and P. Markowski, 2013: Dynamical influences of anvil shading on simulated supercell thunderstorms. *Mon. Wea. Rev.,* **141,** 2802–2820, doi:10.1175/MWR-D-12-00146.1.

French, M. M., L. J. Wicker, D. W. Burgess, and E. R. Mansell, 2014: Mobile, polarimetric Doppler radar observations of supercell hook echoes during VORTEX2. *Special Symp. on Severe Local Storms: The Current State of the Science and Understanding Impacts,* Atlanta, GA, Amer. Meteor. Soc., 817. [Available online at https://ams.confex.com/ams/94Annual/webprogram/Paper236201.html.]

——, D. W. Burgess, E. R. Mansell, and L. J. Wicker, 2015: Hook echo raindrop sizes retrieved using mobile, polarimetric Doppler radar observations. *J. Appl. Meteor. Climatol.,* **54,** 423–450, doi:10.1175/JAMC-D-14-0171.1.

Grzych, M. L., B. D. Lee, and C. A. Finley, 2007: Thermodynamic analysis of supercell rear-flank downdrafts from project ANSWERS. *Mon. Wea. Rev.,* **135,** 240–246, doi:10.1175/MWR3288.1.

Harrington, J. Y., K. J. Sulia, and H. Morrison, 2013: A method for adaptive habit prediction in bulk microphysical models. Part I: Theoretical development. *J. Atmos. Sci.,* **70,** 349–364, doi:10.1175/JAS-D-12-040.1.

Hashino, T., and G. J. Tripoli, 2007: The Spectral Ice Habit Prediction System (SHIPS). Part I: Model description and simulation of the vapor deposition process. *J. Atmos. Sci.,* **64,** 2210–2237, doi:10.1175/JAS3963.1.

Klemp, J. B., and R. Rotunno, 1983: A study of the tornadic region within a supercell thunderstorm. *J. Atmos. Sci.,* **40,** 359–377, doi:10.1175/1520-0469(1983)040<0359:ASOTTR>2.0.CO;2.

Kosiba, K., J. Wurman, Y. P. Richardson, P. M. Markowski, P. Robins, and J. Marquis, 2013: Genesis of the Goshen County, Wyoming, tornado on 5 June 2009 during VORTEX2. *Mon. Wea. Rev.,* **141,** 1157–1181, doi:10.1175/MWR-D-12-00056.1.

Kumjian, M. R., 2011: Precipitation properties of supercell hook echoes. *Electron. J. Severe Storms Meteor.,* **6** (5). [Available online at http://ejssm.org/ojs/index.php/ejssm/article/viewArticle/93.]

——, and A. V. Ryzhkov, 2008a: Microphysical differences between tornadic and nontornadic supercell rear-flank downdrafts revealed by dual-polarization radar measurements. *24th Conf. on Severe Local Storms,* Savannah, GA, Amer. Meteor. Soc., 3B.4. [Available online at https://ams.confex.com/ams/24SLS/techprogram/paper_141912.htm.]

——, and ——, 2008b: Polarimetric signatures in supercell thunderstorms. *J. Appl. Meteor. Climatol.,* **47,** 1940–1961, doi:10.1175/2007JAMC1874.1.

——, and ——, 2009: Storm-relative helicity revealed from polarimetric radar observations. *J. Atmos. Sci.,* **66,** 667–685, doi:10.1175/2008JAS2815.1.

——, and ——, 2012: The impact of size sorting on the polarimetric radar variables. *J. Atmos. Sci.,* **69,** 2042–2060, doi:10.1175/JAS-D-11-0125.1.

——, and O. P. Prat, 2014: The impact of raindrop collisional processes on the polarimetric radar variables. *J. Atmos. Sci.,* **71,** 3052–3067, doi:10.1175/JAS-D-13-0357.1.

Lebo, Z. J., H. Morrison, and J. H. Seinfeld, 2012: Are simulated aerosol-induced effects on deep convective clouds strongly dependent on saturation adjustment? *Atmos. Chem. Phys.,* **12,** 9941–9964, doi:10.5194/acp-12-9941-2012.

Lee, B. D., C. A. Finley, and T. M. Samaras, 2011: Surface analysis near and within the Tipton, Kansas, tornado on 29 May 2008. *Mon. Wea. Rev.,* **139,** 370–386, doi:10.1175/2010MWR3454.1.

——, ——, and C. D. Karstens, 2012: The Bowdle, South Dakota, cyclic tornadic supercell of 22 May 2010: Surface analysis of rear-flank downdraft evolution and multiple internal surges. *Mon. Wea. Rev.,* **140,** 3419–3441, doi:10.1175/MWR-D-11-00351.1.

Loftus, A. M., W. R. Cotton, and G. G. Carrió, 2014: A triple-moment hail bulk microphysics scheme. Part I: Description and initial evaluation. *Atmos. Res.,* **149,** 35–57, doi:10.1016/j.atmosres.2014.05.013.

Mansell, E. R., 2010: On sedimentation and advection in multimoment bulk microphysics. *J. Atmos. Sci.,* **67,** 3084–3094, doi:10.1175/2010JAS3341.1.

Markowski, P. M., 2002: Hook echoes and rear-flank downdrafts: A review. *Mon. Wea. Rev.,* **130,** 852–876, doi:10.1175/1520-0493(2002)130<0852:HEARFD>2.0.CO;2.

——, and Y. P. Richardson, 2014: The influence of environmental low-level shear and cold pools on tornadogenesis: Insights from idealized simulations. *J. Atmos. Sci.,* **71,** 243–275, doi:10.1175/JAS-D-13-0159.1.

——, J. M. Straka, and E. N. Rasmussen, 2002: Direct surface thermodynamic observations within the rear-flank downdrafts of nontornadic and tornadic supercells. *Mon. Wea. Rev.,* **130,** 1692–1721, doi:10.1175/1520-0493(2002)130<1692:DSTOWT>2.0.CO;2.

——, ——, and ——, 2003: Tornadogenesis resulting from the transport of circulation by a downdraft: Idealized numerical simulations. *J. Atmos. Sci.,* **60,** 795–823, doi:10.1175/1520-0469(2003)060<0795:TRFTTO>2.0.CO;2.

——, Y. P. Richardson, and G. Bryan, 2014: The origins of vortex sheets in a simulated supercell thunderstorm. *Mon. Wea. Rev.,* **142,** 3944–3954, doi:10.1175/MWR-D-14-00162.1.

Milbrandt, J. A., and M. K. Yau, 2005a: A multimoment bulk microphysics parameterization. Part I: Analysis of the role of the spectral shape parameter. *J. Atmos. Sci.,* **62,** 3051–3064, doi:10.1175/JAS3534.1.

——, and ——, 2005b: A multimoment bulk microphysics parameterization. Part II: A proposed three-moment closure and scheme description. *J. Atmos. Sci.,* **62,** 3065–3081, doi:10.1175/JAS3535.1.

——, and R. McTaggart-Cowan, 2010: Sedimentation-induced errors in bulk microphysics schemes. *J. Atmos. Sci.,* **67,** 3931–3948, doi:10.1175/2010JAS3541.1.

Miller, L. J., J. D. Tuttle, and C. A. Knight, 1988: Airflow and hail growth in a severe Northern Plains supercell. *J. Atmos. Sci.,* **45,** 736–762, doi:10.1175/1520-0469(1988)045<0736:AAHGIA>2.0.CO;2.

Mishchenko, M. I., 2000: Calculation of the amplitude matrix for a nonspherical particle in a fixed orientation. *Appl. Opt.,* **39,** 1026–1031, doi:10.1364/AO.39.001026.

Morrison, H., and J. Milbrandt, 2011: Comparison of two-moment bulk microphysics schemes in idealized supercell thunderstorm simulations. *Mon. Wea. Rev.,* **139,** 1103–1130, doi:10.1175/2010MWR3433.1.

——, and J. A. Milbrandt, 2015: Parameterization of cloud microphysics based on the prediction of bulk ice particle properties. Part I: Scheme description and idealized tests. *J. Atmos. Sci.,* **72,** 287–311, doi:10.1175/JAS-D-14-0065.1.

——, J. A. Curry, and V. I. Khvorostyanov, 2005: A new double-moment microphysics parameterization for application in cloud and climate models. Part I: Description. *J. Atmos. Sci.,* **62,** 1665–1677, doi:10.1175/JAS3446.1.

——, G. Thompson, and V. Tatarskii, 2009: Impact of cloud microphysics on the development of trailing stratiform precipitation in a simulated squall line: Comparison of one- and two-moment schemes. *Mon. Wea. Rev.,* **137,** 991–1007, doi:10.1175/2008MWR2556.1.

——, S. A. Tessendorf, K. Ikeda, and G. Thompson, 2012: Sensitivity of a simulated midlatitude squall line to parameterization of raindrop breakup. *Mon. Wea. Rev.,* **140,** 2437–2460, doi:10.1175/MWR-D-11-00283.1.

Rasmussen, R. M., and A. J. Heymsfield, 1987: Melting and shedding of graupel and hail. Part I: Model physics. *J. Atmos. Sci.,* **44,** 2754–2763, doi:10.1175/1520-0469(1987)044<2754:MASOGA>2.0.CO;2.

——, V. Levizzani, and H. R. Pruppacher, 1984: A wind tunnel and theoretical study on the melting behavior of atmospheric ice particles: III. Experiment and theory for spherical ice particles of radius > 500 μm. *J. Atmos. Sci.,* **41,** 381–388, doi:10.1175/1520-0469(1984)041<0381:AWTATS>2.0.CO;2.

Ryzhkov, A. V., M. R. Kumjian, S. M. Ganson, and A. P. Khain, 2013: Polarimetric radar characteristics of melting hail. Part I: Theoretical simulations using spectral microphysical modeling. *J. Appl. Meteor. Climatol.,* **52,** 2849–2870, doi:10.1175/JAMC-D-13-073.1.

Schenkman, A. D., M. Xue, and A. Shapiro, 2012: Tornadogenesis in a simulated mesovortex within a mesoscale convective system. *J. Atmos. Sci.,* **69,** 3372–3390, doi:10.1175/JAS-D-12-038.1.

——, ——, and M. Hu, 2014: Tornadogenesis in a high-resolution simulation of the 8 May 2003 Oklahoma City supercell. *J. Atmos. Sci.,* **71,** 130–154, doi:10.1175/JAS-D-13-073.1.

Schuur, T. J., A. V. Ryzhkov, D. S. Zrnić, and M. Schönhuber, 2001: Drop size distributions measured by a 2D video disdrometer: Comparison with dual-polarization radar data. *J. Appl. Meteor.,* **40,** 1019–1034, doi:10.1175/1520-0450(2001)040<1019:DSDMBA>2.0.CO;2.

Seifert, A., and K. D. Beheng, 2001: A double-moment parameterization for simulating autoconversion, accretion, and self-collection. *Atmos. Res.,* **59–60,** 265–281, doi:10.1016/S0169-8095(01)00126-0.

Skamarock, W. C., and Coauthors, 2008: A description of the Advanced Research WRF version 3. NCAR Tech. Note NCAR/TN-475+STR, 113 pp. [Available online at http://www.mmm.ucar.edu/wrf/users/docs/arw_v3_bw.pdf.]

Van Den Broeke, M. S., 2014: Effects of mid- and upper-level dry layers on microphysics of simulated supercell storms. *Electron. J. Severe Storms Meteor.,* **9** (3). [Available online at http://www.ejssm.org/ojs/index.php/ejssm/article/viewFile/134/99.]

——, J. M. Straka, and E. Rasmussen, 2010: Mesocyclone and RFD evolution in simulated supercell storms with varying wind profiles. *25th Conf. on Severe Local Storms,* Denver, CO, Amer. Meteor. Soc., 8A.6. [Available online at https://ams.confex.com/ams/pdfpapers/175853.pdf.]

Wacker, U., and A. Seifert, 2001: Evolution of rain water profiles resulting from pure sedimentation: Spectral vs. parameterized description. *Atmos. Res.,* **58,** 19–39, doi:10.1016/S0169-8095(01)00081-3.

Weisman, M. L., and J. B. Klemp, 1982: The dependence of numerically simulated convective storms on vertical wind shear and buoyancy. *Mon. Wea. Rev.,* **110,** 504–520, doi:10.1175/1520-0493(1982)110<0504:TDONSC>2.0.CO;2.

——, and R. Rotunno, 2000: The use of vertical wind shear versus helicity in interpreting supercell dynamics. *J. Atmos. Sci.,* **57,** 1452–1472, doi:10.1175/1520-0469(2000)057<1452:TUOVWS>2.0.CO;2.

Wurman, J., D. Dowell, Y. P. Richardson, P. M. Markowski, E. N. Rasmussen, D. W. Burgess, L. J. Wicker, and H. B. Bluestein, 2012: The Second Verification of the Origins of Rotation in Tornadoes Experiment: VORTEX2. *Bull. Amer. Meteor. Soc.,* **93,** 1147–1170, doi:10.1175/BAMS-D-11-00010.1.